Nanoscale

ROYAL SOCIETY OF CHEMISTRY

PAPER

View Article Online
View Journal | View Issue

Cite this: *Nanoscale*, 2023, **15**, 17206

In situ assembly of one-dimensional Pt@ZnO nanofibers driven by a ZIF-8 framework for achieving a high-performance acetone sensor†

Zaiping Chen, Wei Liu, * Xiaohui Si, Junmeng Guo, Jiahang Huo, Zhiheng Zhang, Gang Cheng * and Zuliang Du

To obtain a high-performance gas sensor, it is essential to ingeniously design sensing materials containing the features of high catalytic performance, abundant oxygen vacancies, and splendid grain dispersibility through a simple method. Inspired by the fact that ZIF-8 contains semiconductor metal atoms, well-arranged ZnO nanoparticle (NP)-*in situ* assembled one-dimensional nanofibers (NFs) are obtained by one-step electrospinning. By incorporating Pt NPs into the cavity of ZIF-8 NPs, well-dispersed Pt@ZnO NPs driven by Pt@ZIF-8 composites are obtained after annealing. The well-arranged Pt@ZnO NP-assembled NFs not only exhibit abundant oxygen vacancies but also avoid the self-aggregation of ZnO and Pt NPs. Meanwhile, the small Pt NPs could improve the catalytic effect in return. Therefore, the gas sensor fabricated based on the above materials exhibits an acetone sensitivity of 6.1 at 370 °C, compared with pristine ZnO NFs (1.6, 5 ppm). Moreover, the well-arranged Pt@ZnO NP-assembled NFs show exceptional sensitivity to acetone with a 70.2 ppb-level detection limit in theory. The synergistic advantages of the designed sensing material open up new possibilities for non-invasive disease diagnosis.

Received 12th August 2023,
Accepted 6th October 2023

DOI: 10.1039/d3nr04040b

rsc.li/nanoscale

1. Introduction

Chemiresistors have been proved to be promising gas sensors for applications in environmental monitoring, artificial intelligence, and breath detection because of their tunability, high sensitivity, and low cost.[1–4] The sensing performance of chemiresistors mainly relies on their sensing materials.[5] Consequently, for achieving high-performance gas sensors, researchers are now focused on the development of advanced sensing materials.[6] Among practical contenders, ZIF-8 is regarded as the most representative metal–organic frame (MOF) material for gas sensors thanks to its abundant microporous structure, distinguished physical and chemical stability, excellent confinement effect, and plenty of active sites.[7–11] However, due to low internal resistance channels and large barrier heights, single-component structures usually have inferior gas-sensing properties compared to multi-component structures.[12]

To solve the above problems, researchers have used heterojunctions and noble metal doping to improve the gas sensing performance. For example, Chen *et al.*[13] fabricated a novel SnO_2–SnO nanostructure with a p–n heterojunction, which possesses excellent gas sensing properties for NO_2. Furthermore, Chen *et al.*[14] synthesized a Pd doped $W_{18}O_{49}$ nanowire structure with heterostructures and abundant oxygen vacancies, which exhibits excellent gas sensing behavior for acetone. Therefore, among the most effective solutions to the above problem is adding noble metal catalysts, which can be functionalized on sensing materials.[15,16] However, small-size noble metal NPs are thermodynamically unstable and prone to agglomerate into larger particles at high temperatures, which reduces their exposed active sites.[17] Combining the confinement effect of the ZIF-8 microporous structure to stabilize noble metal NPs can effectively solve the above problem.[18,19] Because of the confinement by the rigid organic ligand framework and improved support–metal interaction, the noble metal NPs within ZIF-8 are restrained from relocating, which would provide the following superiorities: (1) the noble metal NPs preserve the good dispersion within the cavity of ZIF-8 during the synthetic process; (2) the well-dispersed structure is beneficial to reduce the formation of low-resistance channels and guarantees the maximum exposure of the active sites for the

Key Lab for Special Functional Materials, Ministry of Education, National & Local Joint Engineering Research Center for High-efficiency Display and Lighting Technology, School of Materials Science and Engineering, and Collaborative Innovation Center of Nano Functional Materials and Applications, Henan University, Kaifeng 475004, China. E-mail: weil@henu.edu.cn, chenggang@henu.edu.cn

† Electronic supplementary information (ESI) available. See DOI: https://doi.org/10.1039/d3nr04040b

gas-sensing process; and (3) this strategy allows for *in situ* doping of noble metals and increases the number of lattice defects and oxygen vacancies.[20–22]

In recent decades, numerous studies have been performed on sensing materials to enhance gas sensing performance.[23–25] Especially, the strategy of employing one-dimensional (1D) nanostructures is extremely beneficial for gas sensors owing to the adequate reaction region between the active sites and the analytes and the favorable electron transport structure.[26] However, the synthesis of 1D structures typically involves heating procedures, which results in non-uniform grain sizes because of the aggregation of small particles. Large grains severely restrict the sensitivity of the sensing materials due to the low reactivity, incomplete depletion region, and good conductivity. Therefore, electricity easily passes across larger grains, leading to the formation of low-resistance channels and hindering the promotion of gas-sensing properties.[27–29]

To address these issues, we report an interesting electrospinning and annealing method for designing NFs, which uses Pt@ZIF-8 NP-driven well-aligned Pt@ZnO NPs as NF assemblies. Simple diffusion of Pt ions into the cavity of ZIF-8 NPs, followed by embedding into electrospun polyacrylonitrile (PAN) after reduction by sodium borohydride, and subsequent annealing result in Pt@ZnO NP composite NFs. The final Pt@ZnO NFs as a sensing material not only well-restricted the self-agglomeration of Pt and ZnO grains but also produced a nanofibrous morphology for reducing low-resistance channels. Benefiting from the hierarchical well-arranged morphology and the low Pt catalyst level, these Pt@ZnO NFs display terrific acetone sensing properties and even better sensitivity and robustness than those reported in many studies.

2. Experimental section

2.1 Synthesis of ZIF-8 NPs

First, 6.56 g of 2-methylimidazole and 2.95 g of zinc nitrate hexahydrate were dissolved in 200 mL of methanol, respectively, and then kept under magnetic stirring for 10 min. Then, zinc nitrate hexahydrate solution was injected quickly into the 2-methylimidazole solution and magnetically stirred for another 2 h. After centrifugation (10 000 rpm, 3 min), the ZIF-8 NPs were washed with methanol (3 times) and dried at 80 °C overnight.

2.2 Synthesis of Pt@ZIF-8 NPs

First, 1 g of ZIF-8 NPs was blended with 5 mL of methanol for 48 h, and then the mixture was sonicated for 3 h to form a uniform solution. Then, the as-prepared solution (1 mL) was added to deionized water (1 mL) and magnetically stirred for 15 min. Then, 160 μL, 320 μL, and 955 μL of chloroplatinic acid hexahydrate solution (1.6 mg mL^{-1}) were added to the above solution and stirred for 1 h, respectively. Subsequently, Pt ions were reduced to Pt in the framework of ZIF-8 *via* the reducing action of $NaBH_4$ solution (1.5 mg mL^{-1}). After centrifugation (10 000 rpm, 15 min), the as-prepared sample was washed with methanol (3 times) and dried at 60 °C overnight.

2.3 Synthesis of Pt@ZnO NFs

First, 0.1563 g of Pt@ZIF-8 NPs were added to 2.065 g of *N*,*N*-dimethylformamide (DMF) and sonically dispersed for 30 min. Then a uniform precursor solution was prepared by injecting 0.175 g of polyacrylonitrile (PAN) into the solvent and stirring continuously for 24 h. Then, the mixed solution was injected into a 5 mL syringe for electrospinning (the voltage is 20 kV, the feeding rate is 2 mL h^{-1} and the speed of the rotating drum receiver is 260 rpm) and then dried at 70 °C overnight. The Pt@ZIF-8/PAN NFs were calcined at 700 °C for 2 h (2 °C min^{-1}) in a tube furnace. Finally, the Pt@ZnO NFs with different Pt contents (0.005 wt%, 0.01 wt%, and 0.03 wt%) were obtained and named 5-Pt, 10-Pt, and 30-Pt, respectively.

2.4 Sensor fabrication

To obtain the sensing layer, the Pt@ZnO NFs were blended with ethanol and coated with a brush on a ceramic tube. Then, the ceramic tube was calcined at 350 °C for 2 h (2 °C min^{-1}). After calcination, Ni–Cr heating wires were inserted into the ceramic tube and aged for 2 weeks at 350 °C, which is the operating temperature of the gas sensor. A WS-30B (Zhengzhou, China) gas sensing system was used to evaluate the sensing performance of the gas sensor. Gas-sensing properties were evaluated by injecting a standard gas into the sealed chamber (18 L). The resistance ratio (R_a/R_g) represents the sensor's response value, R_a represents the resistance in air, and R_g represents the resistance in the target gas. The concentration of the target gas obtained from acetone (C_3H_6O) was calculated using eqn (1):

$$V_x = \frac{V \times C \times M}{22.4 \times d \times p} \times 10^{-9} \times \frac{273 + T_r}{273 + T_b} \quad (1)$$

In the equation, V_x (μL) represents the liquid volume, V (mL) represents the testing chamber volume, C (ppm) represents the liquid vapor concentration, M (g) represents the liquid molecular weight, d (g cm^{-3}) represents the liquid specific gravity, p represents the purity of the liquid, T_r (°C) represents the ambient temperature and T_b (°C) represents the test chamber temperature. The ambient temperature and relative humidity were 23 °C and 25%, respectively.

3. Results and discussion

3.1 Morphologies and structural properties

The schematic illustration of the route for the preparation of Pt@ZnO NFs, which were prepared from small-size Pt NPs and well-aligned ZnO NPs, is depicted in Fig. 1. First, Pt^{4+} ions with a radius of 0.625 Å[30] were diffused into the ZIF-8 cavity (11.6 Å). After that, the Pt^{4+} ions in the cavity were reduced to Pt using $NaBH_4$. The obtained Pt@ZIF-8 NPs were embedded into PAN NFs *via* electrospinning. Then, the prepared Pt@ZIF-8/PAN NFs were vacuum-dried to accelerate solvent evaporation and facilitate stripping of the Pt@ZIF-8/PAN NFs from the substrate. Finally, ZIF-8 was reduced to the ZnO framework and the small-size Pt NPs were retained in the ZnO

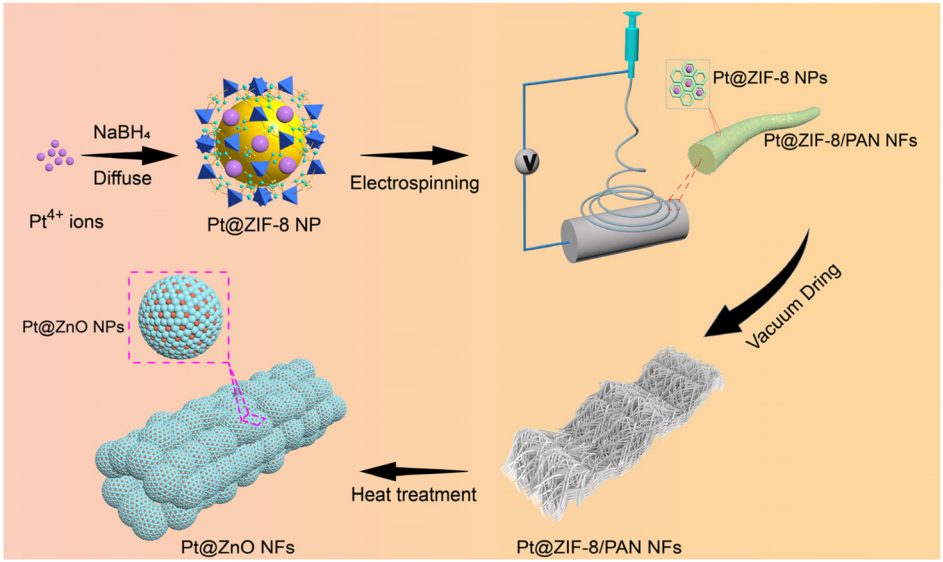

Fig. 1 Schematic diagram of the process for the preparation of Pt@ZnO NFs.

framework, and then NFs were calcined in air at 700 °C. A large mass loss occurred within the interconnected Pt@ZIF-8 particles, resulting in the formation of the well-arranged Pt@ZnO NP-assembled NFs.

As shown in Fig. 2a, scanning electron microscopy (SEM) revealed that the morphology of Pt@ZIF-8 NPs was characterized by small and sharp hexagonal planes with an average particle size of about 38 nm (Fig. S1†). The retention of Pt NPs

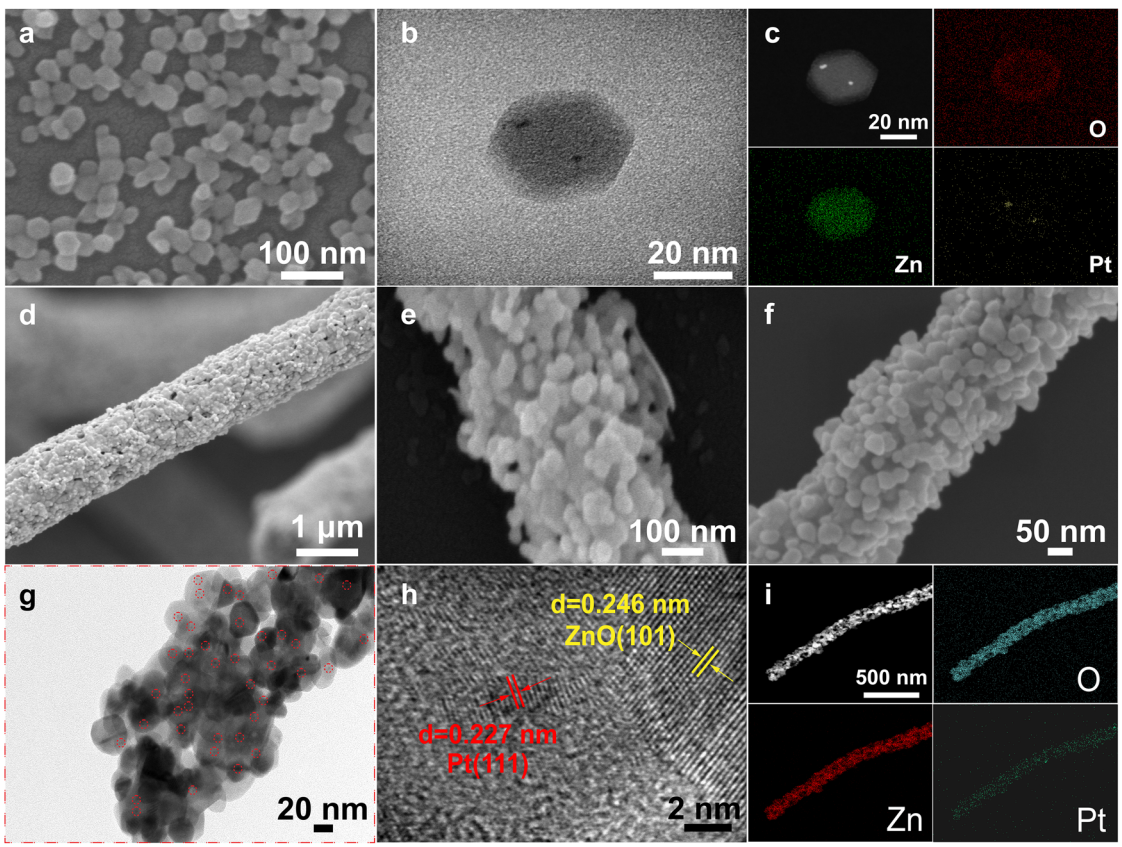

Fig. 2 (a) SEM image, (b) TEM image and (c) EDX elemental mapping images of Pt@ZIF-8 NPs. SEM images of (d) ZIF-8/PAN NFs, (e) pristine ZnO NFs and (f) Pt@ZnO NFs. (g) TEM image, (h) HRTEM image and (i) EDX elemental mapping images of Pt@ZnO NFs.

(3.6 nm) within the ZnO framework was further confirmed by transmission electron microscopy (TEM) and energy dispersive X-ray (EDX) mapping images of Pt@ZIF-8 NPs (Fig. 2b and c, Fig. S2†). As shown in Fig. 2d, ZIF-8/PAN NFs are characterized by a long, uniform structure with a diameter of 840 nm, whereas the diameter of pristine ZnO NFs (440 nm) shrinks after heating treatment (Fig. 2e). The morphology of the arranged ZnO NPs showed no self-aggregation in contrast to ZnO NFs without ZIF-8 NPs as a driver (Fig. S3†). In fact, the existence of Pt NPs has an effect on the catalytic activity and causes lattice distortion of ZnO particles in the crystal growth stage, which inhibits grain boundary migration and increases the energy barrier of grain growth.[31–33] Meanwhile, noble metals have been shown to effectively prevent SMO particle grain growth,[34] resulting in the further reduction of the diameter (255 nm) of Pt@ZnO NFs (Fig. 2f, Fig. S4†). In addition, the Pt@ZnO NFs with different Pt amounts were investigated using the X-ray diffraction (XRD) pattern (Fig. S5†). The grain sizes of pristine ZnO NFs, 5-Pt, 10-Pt, and 30-Pt were calculated to be 17.20 nm, 16.07 nm, 16.63 nm and 15.95 nm with Scherrer's formula, respectively, consistent with the hexagonal fibrillated zincite structure of ZnO (PDF#89-0511). No diffraction peak of platinum was observed due to the very little addition, and the specific surface area was barely changed (Fig. S6†).

The effect of annealing temperature on Pt@ZnO NFs was clearly investigated using the temperature gradient of 200 °C–900 °C (Fig. S7†). When the annealing temperature was 200 °C–600 °C, a smooth and flaky morphology of Pt@ZnO NFs can result from the poor crystallization of ZnO and the incomplete decomposition of the PAN matrix. Once the annealing temperature reached 700 °C, the well-arranged Pt@ZnO NPs can be viewed along the whole NFs. With the increase of the heating temperature (800 °C–900 °C), the Pt@ZnO NPs gradually agglomerated into larger particles. The XRD pattern (Fig. S8†) revealed that the Pt@ZnO NFs at 700 °C exhibit better crystallinity than at other heating temperatures. The nanoscale structure and chemical characterization were studied *via* TEM images. Fig. 2g shows that the prepared Pt@ZnO NFs exhibit a long and uniform structure, and small-size Pt NPs (red circle) are observed on the whole Pt@ZnO NFs, indicating that the Pt NPs have not self-agglomerated after the thermal treatment. As shown in Fig. 2h, in the high-resolution transmission electron microscopy (HRTEM) image of Pt@ZnO NFs, distinct lattice fringes can be observed with crystal plane spacing of 0.246 nm and 0.227 nm, corresponding to the ZnO (101) crystal plane of the wurtzite phase and the Pt (111) crystal plane of the cubic phase, respectively. In addition, the EDX mapping images of Pt@ZnO NFs reveal that O, Zn, and Pt elements are well-distributed on the whole NFs, further demonstrating the uniform dispersion of small-size Pt NPs in the ZnO framework and that Pt@ZnO NPs are uniformly arranged on the entire NFs (Fig. 2i).

To study the variation of oxygen defects, UV absorption spectroscopy was performed on pristine ZnO NFs and Pt@ZnO NFs in the range of 300–800 nm (Fig. 3a). The pristine ZnO NFs showed an absorption peak at 374 nm with a band gap of 2.99 eV according to the Tauc plot (Fig. 3a). Additionally, Pt@ZnO NFs with increasing Pt NP loading have a lower band gap value. This can result from the excess defects induced by Pt NPs in the band gap of ZnO.[35,36] The results are consistent with the room temperature photoluminescence (PL) spectra shown in Fig. 3b. In the visible region, different NFs have different peak intensities due to different oxygen vacancies on their surfaces.[37] The 10-Pt sample displayed the highest peak intensity, proving that it had the maximum number of oxygen vacancies compared to the other samples.

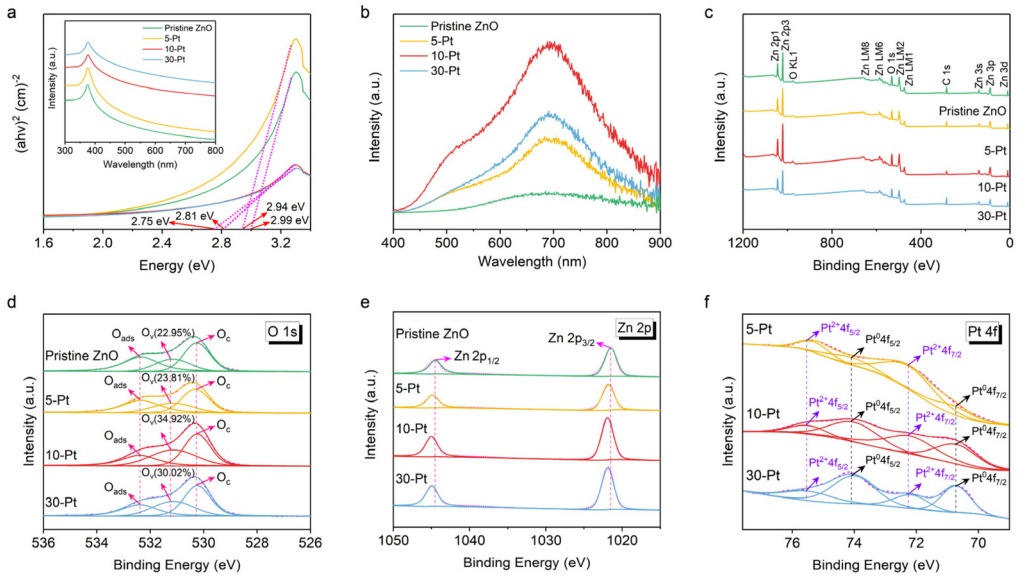

Fig. 3 (a) Tauc plot and UV absorption spectra, (b) PL spectra, (c) survey XPS spectra, (d) O 1s XPS spectra and (e) Zn 2p XPS spectra of pristine ZnO, 5-Pt, 10-Pt and 30-Pt. (f) Pt 4f XPS spectra of 5-Pt, 10-Pt and 30-Pt.

The chemical states and elemental compositions of ZnO NFs with different Pt contents were analyzed by X-ray photoelectron spectroscopy (XPS). The results showed the coexistence of O and Zn elements (Fig. 3c). The XPS spectra of O 1s can be fitted into three peaks, which are located at 530.26 eV attributed to crystal lattice oxygen (O_c), at 531.15 eV attributed to deficient oxygen (O_v) and at 532.37 eV attributed to adsorbed oxygen (O_{ads}), respectively (Fig. 3d). The results revealed that Pt catalysts greatly increase the amount of oxygen filling and generation rate of vacancies on the surface of NFs due to the spillover effect,[38] and the proportion of oxygen vacancies is much higher in Pt@ZnO NFs than in pristine ZnO NFs. Fig. 3d shows that the oxygen vacancy ratios of pristine ZnO, 5-Pt, 10-Pt, and 30-Pt are 22.95%, 23.81%, 34.92%, and 30.02%, respectively, and the 10-Pt sample exhibits the largest oxygen vacancy ratio compared to the other three samples. A large oxygen vacancy ratio is the key factor of sensing materials for achieving superior gas-sensing properties. In addition, the peak at 1021.74 eV corresponds to Zn $2p_{3/2}$ of ZnO, and the peak at 1044.79 eV corresponds to Zn $2p_{1/2}$ of ZnO (Fig. 3e), further demonstrating that ZIF-8 NPs are converted into ZnO NPs after calcination. The peak positions of Pt@ZnO NFs exhibited a significant redshift relative to those of pristine ZnO NFs, which confirmed the electronic interaction (electrons transfer from ZnO to Pt) between Pt and ZnO.[39,40] Fig. 3f shows the Pt 4f XPS spectra of 5-Pt, 10-Pt, and 30-Pt, respectively. The XPS spectra of Pt 4f can be fitted into four peaks and the ratio of Pt $4f_{7/2}$ to Pt $4f_{5/2}$ is 4 : 3, the Pt $4f_{5/2}$ (74.05 eV) and Pt $4f_{7/2}$ (70.75 eV) of the Pt elemental state, and the Pt $4f_{5/2}$ (75.50 eV) and Pt $4f_{7/2}$ (72.20 eV) of the Pt^{2+} state,[41] respectively, and it indicated that Pt NPs had oxidized partially. Moreover, the Pt NPs were not further oxidized under the protection of the ZnO framework, no Pt^{4+} state was observed, and the spin–orbit coupling energy between all Pt $4f_{5/2}$ and $4f_{7/2}$ is 3.3 eV, which is consistent with the result of a previous study.[42]

3.2 Gas sensing properties towards acetone

Using the four as-prepared samples, we fabricated side-heated gas sensors to demonstrate their gas-sensing characteristics. One of the most significant factors affecting gas sensor sensitivity is operating temperature. The gas sensing characteristics of the four sensors toward 10 ppm acetone were tested between 260 °C and 420 °C. As shown in Fig. 4a, the response values of all sensors first increase and then decrease with the rise of temperature, which is ascribed to insufficient activation energy at low temperatures and superfluous kinetic energy for the reaction of acetone and adsorbed oxygen at high temperatures.[43] The optimal working temperature of pure ZnO is reduced after loading Pt nanoparticles due to the noble metal catalyst decreasing the activation energy of gas chemisorption and increasing adsorbed oxygen species.[44] Furthermore, we can observe that the adsorbed oxygen content is low (Fig. 3d) and the catalytic effect is not obvious in the 5-Pt sample due to the low Pt doping in ZnO. To achieve the best response to acetone, the 5-Pt sensor requires a higher activation energy than the 10-Pt sensor. Therefore, the optimal operating temperature of the 5-Pt sensor is higher than that of the 10-Pt sensor. For the 30-Pt sample, the active sites of ZnO were overlaid due to the excess Pt doping in ZnO, resulting in a lower adsorbed oxygen content than that in the 10-Pt sample.[45] The 10-Pt sensor exhibited the highest acetone response value (10 ppm, R_a/R_g = 10.88) compared with the other three gas sensors at 370 °C, indicating that the optimal operating temperature is 370 °C. Fig. 4b–e show the transient change in R_a

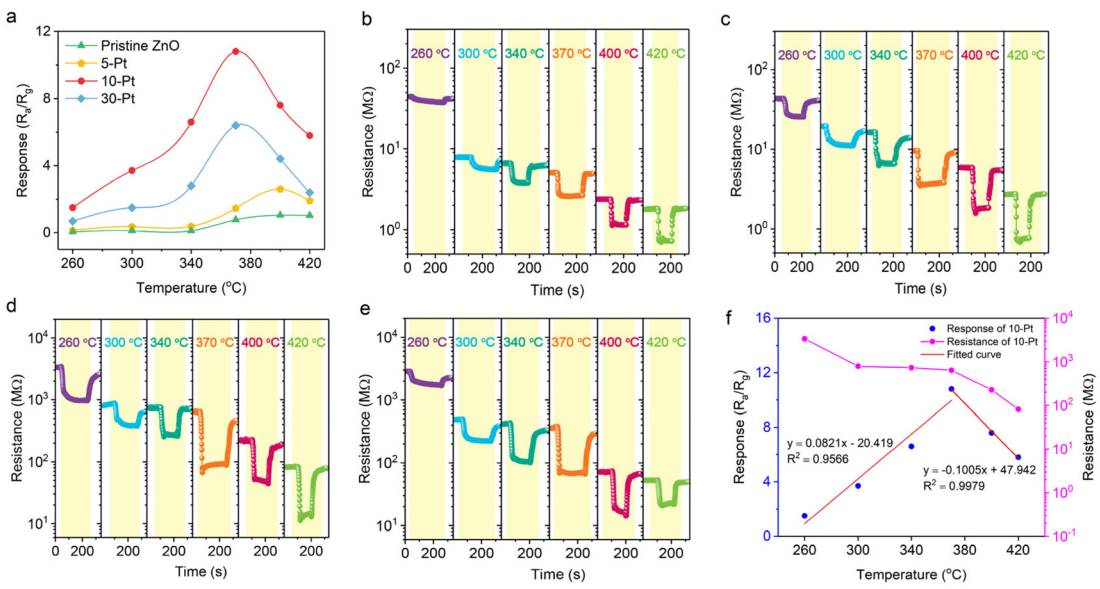

Fig. 4 (a) Response of the as-prepared samples to 10 ppm acetone at different temperatures. The transient change in R_a with operating temperature of (b) pristine ZnO, (c) 5-Pt, (d) 10-Pt and (e) 30-Pt sensors. (f) Response and R_a of the 10-Pt sensor to 10 ppm acetone around the working temperature.

with different operating temperatures of pristine ZnO, 5-Pt, 10-Pt and 30-Pt sensors, and the corresponding variation of R_a values is shown in Fig. S9.† The thermal excitation of electrons in the material enhanced with the increase in operating temperature and more electrons entered the conduction band of sensors, leading to a decrease in R_a, which is consistent with the typical conduction properties of semiconductor materials.[46] In addition, the change in R_a induced by the change in the sensor material at the same operating temperature can be attributed to two major factors. On the one hand, the grain sizes of 5-Pt, 10-Pt, and 30-Pt are much smaller than the two-fold Debye length of pristine ZnO (15 nm) with the addition of Pt NPs.[47] The change of grain sizes affects the intergranular contacts and leads to more grain barriers encountered during electron transfer, resulting in an increase in R_a as the grain sizes decrease.[48] On the other hand, due to the appropriate addition of the Pt catalyst, the Fermi-level of Pt-doped ZnO shifts upward compared with that of pristine ZnO, which allows more electrons to transfer from the conduction band of ZnO to Pt.[49,50] Thus, the change creates an additional depletion layer and significantly increases the R_a of sensors. Moreover, the sensitization enhancement from mild Pt doping was inadequate. In contrast, high-degree doping may overlay the initial active sites of ZnO and expedite the desorption process, hindering the reactions.[51] Additionally, the response of the 10-Pt sensor to 10 ppm acetone (Fig. 4f) and 5–100 ppm acetone (Fig. S10†) at around 370 °C was investigated. From the fitting results, we calculated that a 1 °C temperature increase (decrease) from 260 °C to 370 °C (370 °C to 420 °C) has the same effect on the sensor response as 151.28 ppb (185.186 ppb) acetone concentration change.

Fig. 5a displays the dynamic response–recovery curves of the as-prepared sensors targeting 1–5 ppm acetone at 370 °C. The response value of the 10-Pt sensor was calculated to be 6.1 toward 5 ppm acetone, which was 3.8, 3.4, and 1.4 times higher than that of the pristine ZnO sensor (R_a/R_g = 1.6), the 5-Pt sensor (R_a/R_g = 1.8) and the 30-Pt sensor (R_a/R_g = 4.4), respectively. The results further demonstrated the advantages of small-sized and well-dispersed Pt NPs protected by the ZnO framework. In addition, the resistance of all sensors increases with the increasing concentration of acetone, which is consistent with the response characteristics of n-type semiconductors (Fig. 5b). To confirm that the as-prepared sensor has a wide range of application scenarios, it was tested in a wide concentration range. Fig. 5c shows the dynamic response–recovery curves of the four sensors for 5–100 ppm acetone, and the response value of the 10-Pt based sensor is up to 57.61 at 100 ppm, further demonstrating the extremely wide detection range and high sensitivity. The result is consistent with the response–recovery curves of resistance (Fig. 5d). Fig. 5e shows the linear fit between the response value and different acetone concentrations (1–100 ppm) for the four sensors on the logarithmic scale. Based on the fitted linear curve, R_a/R_g > 1.2 was considered reliable,[52] and the theoretical lower detection limit of the 10-Pt sensor was 70.2 ppb. Moreover, the 10-Pt sensor exhibited a faster response/recovery time (17.1 s/23.9 s) than the pristine ZnO sensor (25.9 s/29.6 s) for 5 ppm acetone (Fig. 5f).

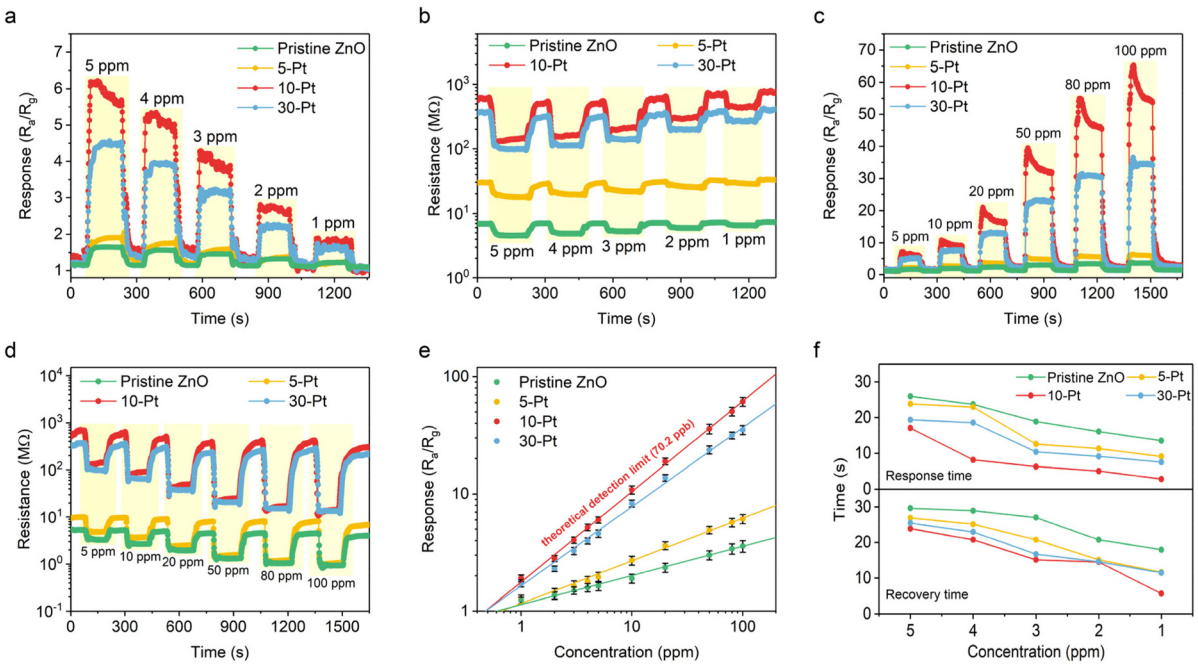

Fig. 5 (a) Dynamic response–recovery curves and (b) dynamic resistance curves of pristine ZnO, 5-Pt, 10-Pt, and 30-Pt sensors at 370 °C for 1–5 ppm acetone. (c) Dynamic response–recovery curves and (d) dynamic resistance curves of pristine ZnO, 5-Pt, 10-Pt, and 30-Pt sensors at 370 °C for 5–100 ppm acetone. (e) Linear fit between acetone concentration (1–100 ppm) and response of pristine ZnO, 5-Pt, 10-Pt, and 30-Pt sensors on the logarithmic scale. (f) Response/recovery time of pristine ZnO, 5-Pt, 10-Pt and 30-Pt sensors for 1–5 ppm acetone.

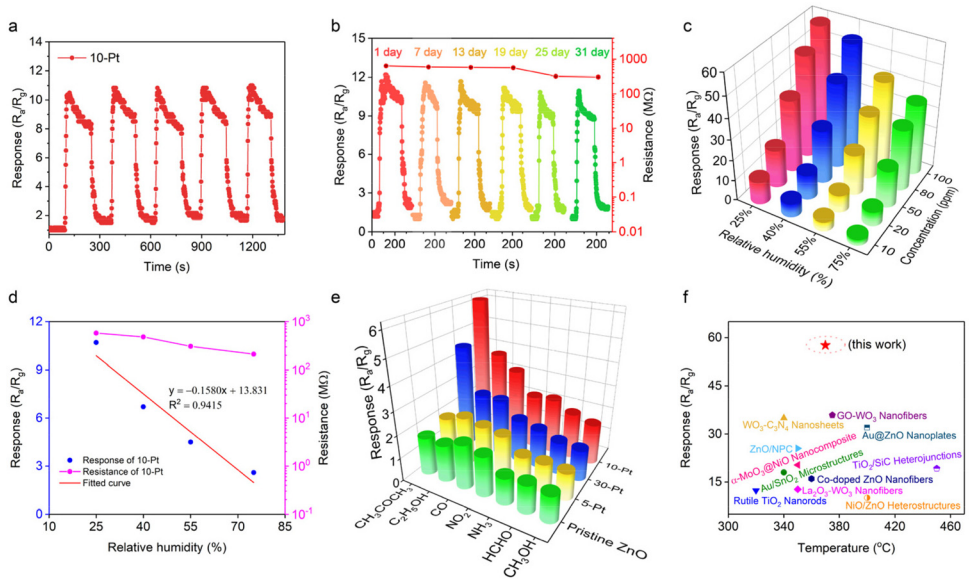

Fig. 6 (a) Repeatability test and (b) long-term stability test of the 10-Pt sensor for 10 ppm acetone at 370 °C. (c) The response of the 10-Pt sensor to 10–100 ppm acetone at various relative humidity levels. (d) The variation of R_a and response values of the 10-Pt sensor *versus* relative humidity. (e) Selectivity test of the 10-Pt sensor to 5 ppm acetone at 370 °C. (f) Comparison of the gas-sensing performance of the 10-Pt sensor with that of the other SMO-based acetone sensors.

Repeatability and stability are the key parameters for evaluating the practicality of gas sensors. As shown in Fig. 6a, the 10-Pt based sensor displayed superior repeatability after five cycles towards 10 ppm acetone, indicating a highly repetitive and stable response and recovery behavior. As shown in Fig. 6b, at least one month of gas-sensitivity testing was conducted on the 10-Pt sensor at an optimum operating temperature for 10 ppm acetone, and it can retain more than 90% of the initial response with no significant baseline drift, confirming its excellent stability and durability. To explore the effect of humidity on the performance of the sensor, the response of the 10-Pt sensor to different concentrations of acetone at different relative humidity (RH) levels is shown in Fig. 6c and Fig. S11.† The decrease of sensor response and R_a with the increase of humidity is due to the competition of water molecules on the surface of the 10-Pt sensor, which decreases the adsorption amount of gas molecules and releases the electrons of the adsorbed oxygen on the surface of ZnO.[53,54] From the fitting results, we calculated that 1% RH change has the same effect on the sensor response as that of the 305.48 ppb acetone concentration change (Fig. 6d). Moreover, the selectivity of the four sensors was tested for 5 ppm acetone, in the presence of HCHO, CH_3OH, C_2H_5OH, CO, NO_2 and NH_3, as shown in Fig. 6e. Apparently, the 10-Pt sensor has high selectivity for acetone with a response value of 6.1 (5 ppm). For other interference analytes at a concentration of 5 ppm, such as HCHO, CH_3OH, C_2H_5OH, CO, NO_2 and NH_3, only a small response ($R_a/R_g < 4$) was obtained. We performed a cross-selectivity test on the 10-Pt sensor to verify that the sensor has good selectivity for acetone. The results indicate that the response values of the 10-Pt sensor to 5 ppm acetone show only minor changes in the gas mixture (Table S1 and Fig. S12†), which proves that the selectivity of the 10-Pt sensor for acetone is not affected by other gases (HCHO, CH_3OH, C_2H_5OH, CO, NO_2, and NH_3). Thus, the 10-Pt sensor can be used for gas detection in complex environments. In addition, the high selectivity of the gas sensing mechanism for acetone gas is attributed to two reasons. On the one hand, the acetone molecule has a large dipole moment compared to other reference gases, which allows strong interactions with unsaturated coordinated oxygen atoms on the surface of metal oxides and leads to selective adsorption, resulting in significant selectivity.[55] On the other hand, the lowest unoccupied molecular orbital energy of acetone gas is similar to the electron energy of adsorbed oxygen at a specific temperature, which enhances the surface chemical reaction between adsorbed oxygen and acetone gas molecules.[56] Thus, the 10-Pt sensor exhibits high selectivity. Besides, the sensing performances of Pt@ZnO NF sensors and other SMO sensors are summarized in Table S2,† and the detection performance of our sensor for acetone (100 ppm) is much higher than that of the other acetone sensors based on ZnO and other types of SMOs reported in the literature (Fig. 6f), indicating that the 10-Pt sensor is beneficial for high-performance detection of acetone.

3.3 Gas sensing mechanism

The enhanced sensing performance of chemiresistors is dependent on the change in resistance caused by the adsorption and reaction process of gas on the surface of the sensitive material.[57,58] The typical surface oxygen adsorption model can explain the gas-sensing mechanism of Pt@ZnO NF sensors.[59] At a certain operating temperature, when Pt@ZnO NF sensors are placed in air, oxygen is adsorbed on the surface of the material and traps electrons into the conduction band of the material through the grain boundaries to form ion-state

adsorbed reactive oxygen.[60–62] As a consequence, the number of carriers in the space charge region decreases. Furthermore, because the electron depletion layer gets thicker, resistance increases.[63] The equations for this reaction are (2)–(5):

$$O_{2(g)} \rightarrow O_{2(ads)} \quad (2)$$

$$O_{2(ads)} + e^- \leftrightarrow O_{2(ads)}{}^- \quad (3)$$

$$O_{2(ads)}{}^- + e^- \leftrightarrow 2O_{(ads)}{}^- \quad (4)$$

$$O_{(ads)}{}^- + e^- \leftrightarrow O_{(ads)}{}^{2-} \quad (5)$$

Operating temperatures of 100 °C–150 °C will result in the formation of O_2^-, 150 °C–200 °C will exhibit mainly O^- formation and above 200 °C will result in the formation of O^{2-}.[64] Therefore, in the operating temperature range of this work, the O^{2-} ion is most likely to react with acetone. Fig. 7a shows that acetone reacts with the adsorbed oxygen which reduces the acetone to CO_2 and H_2O providing electrons to Pt@ZnO NFs, when the sensor is exposed to acetone. The reaction is described in eqn (6):[65]

$$CH_3COCH_{3(ads)} + {}^*8O_{(ads)}{}^{2-} \rightarrow 3CO_{2(gas)} + 3H_2O_{(gas)} + 16e^- \quad (6)$$

In this process, the number of majority carriers increases and the thickness of the electron depletion layer decreases due to the gas being released into the atmosphere after the reaction and the trapped electrons returning to the conduction band, which can enhance gas reactivity (Fig. 7b). Additionally, the material exhibits improved gas sensitivity due to the spillover effect of Pt NPs.[66] The electrons belonging to the conduction band of ZnO will be transferred to Pt due to the work function of Pt being greater than that of ZnO, when Pt is introduced into ZnO. As a result, the thickness of the electron depletion layer is much thicker and the height of the barrier is much higher. The valence band spectra of the sensitive material change significantly at the low energy level (Fig. S13†). The valence band positions of 5-Pt (2.61 eV), 10-Pt (2.54 eV), and 30-Pt (2.58 eV) are red-shifted compared to that of pristine ZnO (2.65 eV), which can result from the formation of surface vacancies by the interaction of Pt with ZnO.[67] The valence band shift of NFs and oxygen vacancies on the surface differ due to the different Pt content, consistent with the PL spectra results. Therefore, when the material is exposed to air, the 10-Pt sensor has more surface-active sites and can adsorb more negative oxygen ions. The gas-sensing performance of the 10-Pt sensor will be significantly improved compared to that of other three sensors. Based on the above observations and discussions, the enhanced performance of the 10-Pt sensor can result from the combined effect of abundant active sites on the NF surface, well-aligned Pt@ZnO NPs and well-dispersed Pt NPs in the ZnO framework.

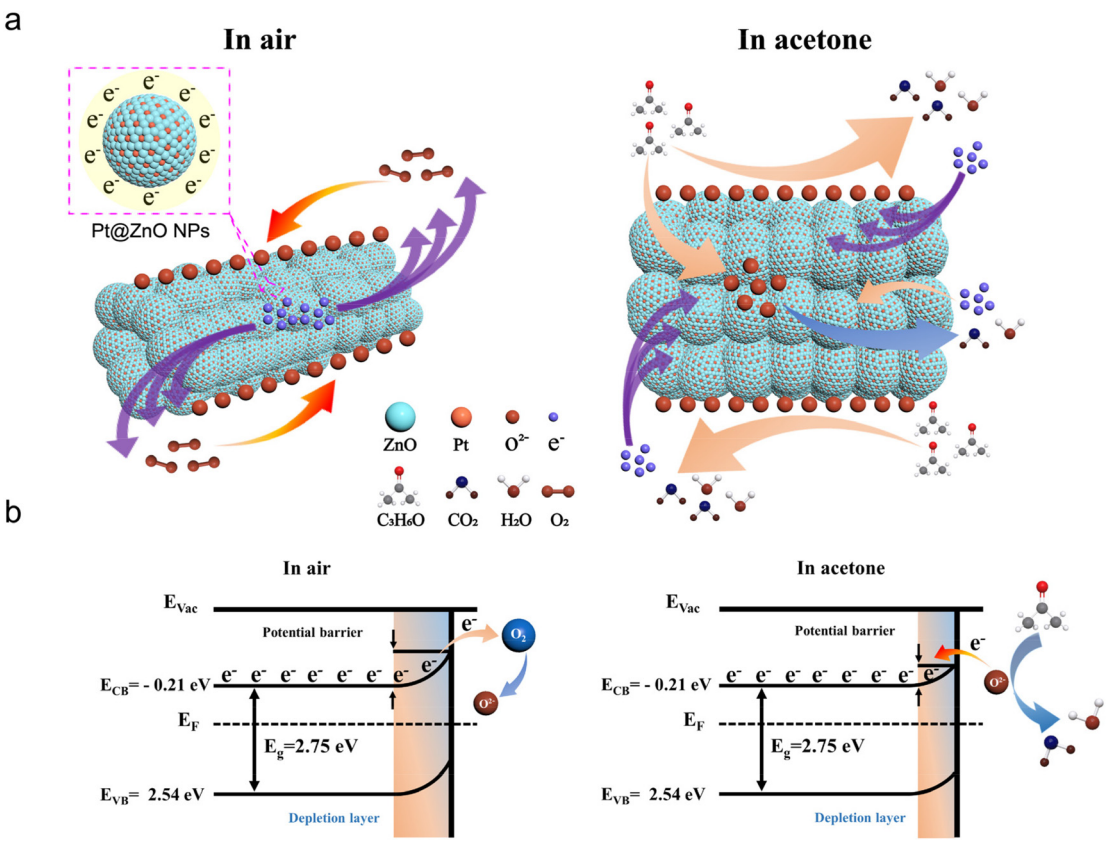

Fig. 7 (a) Adsorption–desorption processes and (b) the energy band structure of the 10-Pt sensor in air and acetone.

4. Conclusions

In summary, we have reported an *in situ* assembly synthetic strategy that could avoid the disadvantages of the traditional method, that is, Pt@ZIF-8-driven Pt@ZnO NPs act as host metal oxide grains, with small-size Pt NPs confined in the ZnO frame, and the following processes of electrospinning and annealing assemble them into the NF morphology. Upon exactly regulating the surface chemistry *via* changing the Pt doping degree and well-arranged Pt@ZnO NPs, the obtained sensing material demonstrated superior properties as an acetone sensor. The well-designed morphology noticeably avoided the self-aggregation of host metal oxide grains and enhanced the interaction between the interface gap and acetone gas. As well as superior selectivity and faster response/recovery time, the response of the 10-Pt sensor is 3.8-fold better than that of the pristine ZnO sensor toward 5 ppm acetone. Hence, the results provide an innovative method to enhance the *in situ* self-assembly of metal oxides to generate excellent gas-sensing properties for applications in various fields.

Conflicts of interest

There are no conflicts to declare.

Acknowledgements

This work was supported by the National Natural Science Foundation of China (62104063 and 61974040) and the China Postdoctoral Science Foundation (2021M701055 and 2022T150188). The authors would also like to thank Shiyanjia Lab (**https://www.shiyanjia.com**) for supporting the XPS analysis.

References

1 Y. Milyutin, M. Abud-Hawa, V. Kloper-Weidenfeld, E. Mansour, Y. Y. Broza, G. Shani and H. Haick, *Nat. Protoc.*, 2021, **16**, 2968–2990.
2 M.-S. Yao, W.-X. Tang, G.-E. Wang, B. Nath and G. Xu, *Adv. Mater.*, 2016, **28**, 5229–5234.
3 M. Guo, J. T. Brewster II, H. Zhang, Y. Zhao and Y. Zhao, *ACS Nano*, 2022, **16**, 17778–17801.
4 H. Shin, D.-H. Kim, W. Jung, J.-S. Jang, Y. H. Kim, Y. Lee, K. Chang, J. Lee, J. Park, K. Namkoong and I.-D. Kim, *ACS Nano*, 2021, **15**, 14207–14217.
5 T. Zhou and T. Zhang, *Small Methods*, 2021, **5**, 2100515.
6 M. V. Nikolic, V. Milovanovic, Z. Z. Vasiljevic and Z. Stamenkovic, *Sensors*, 2020, **20**, 6694.
7 M. Kim, T. Park, C. Wang, J. Tang, H. Lim, M. S. A. Hossain, M. Konarova, J. W. Yi, J. Na, J. Kim and Y. Yamauchi, *ACS Appl. Mater. Interfaces*, 2020, **12**, 34065–34073.
8 K. S. Park, Z. Ni, A. P. Cote, J. Y. Choi, R. Huang, F. J. Uribe-Romo, H. K. Chae, M. O'Keeffe and O. M. Yaghi, *Proc. Natl. Acad. Sci. U. S. A.*, 2006, **103**, 10186–10191.
9 A. Phan, C. J. Doonan, F. J. Uribe-Romo, C. B. Knobler, M. O'keeffe and O. M. Yaghi, *Acc. Chem. Res.*, 2009, **43**, 58–67.
10 J. Hua, C. Li, H. Tao, L. Wang, E. Song, H. Lian, C. Wang, J. Jiang, Y. Pan and W. Xing, *J. Membr. Sci.*, 2021, **636**, 119613.
11 H. Wang, Y. Wang, A. Jia, C. Wang, L. Wu, Y. Yang and Y. Wang, *Catal. Sci. Technol.*, 2017, **7**, 5572–5584.
12 K. M. B. Urs, N. K. Katiyar, R. Kumar, K. Biswas, A. K. Singh, C. S. Tiwary and V. Kamble, *Nanoscale*, 2020, **12**, 11830–11841.
13 L. Li, C. Zhang and W. Chen, *Nanoscale*, 2015, **7**, 12133–12142.
14 P. Li, Z. Zhang, Z. Zhuang, J. Guo, Z. Fang, S. L. Fereja and W. Chen, *Anal. Chem.*, 2021, **93**, 7465–7472.
15 A. Cabot, J. Arbiol, J. R. Morante, U. Weimar, N. Barsan and W. Göpel, *Sens. Actuators, B*, 2000, **70**, 87–100.
16 W. Liu, J. Sun, L. Xu, S. Zhu, X. Zhou, S. Yang, B. Dong, X. Bai, G. Lu and H. Song, *Nanoscale Horiz.*, 2019, **4**, 1361–1371.
17 L. He, Y. Liu, J. Liu, Y. Xiong, J. Zheng, Y. Liu and Z. Tang, *Angew. Chem., Int. Ed.*, 2013, **52**, 3741–3745.
18 S. M. Wu, X. Y. Yang and C. Janiak, *Angew. Chem., Int. Ed.*, 2019, **58**, 12340–12354.
19 K. Zhang, R. P. Lively, C. Zhang, R. R. Chance, W. J. Koros, D. S. Sholl and S. Nair, *J. Phys. Chem. Lett.*, 2013, **4**, 3618–3622.
20 M. Hu, S. Zhao, S. Liu, C. Chen, W. Chen, W. Zhu, C. Liang, W.-C. Cheong, Y. Wang, Y. Yu, Q. Peng, K. Zhou, J. Li and Y. Li, *Adv. Mater.*, 2018, **30**, 1801878.
21 X. Zhou, X. Lin, S. Yang, S. Zhu, X. Chen, B. Dong, X. Bai, X. Wen, L. Geyu and H. Song, *Sens. Actuators, B*, 2020, **309**, 127802.
22 Y. Kang, L. Zhang, W. Wang and F. Yu, *Sensors*, 2021, **21**, 4352.
23 D. Zhang, Z. Yang, S. Yu, Q. Mi and Q. Pan, *Coord. Chem. Rev.*, 2020, **413**, 213272.
24 R. Kumar, X. Liu, J. Zhang and M. Kumar, *Nano-Micro Lett.*, 2020, **12**, 164.
25 C. Zhang, G. Liu, X. Geng, K. Wu and M. Debliquy, *Sens. Actuators, A*, 2020, **309**, 112026.
26 T. Zhang, S. Mubeen, N. V. Myung and M. A. Deshusses, *Nanotechnology*, 2008, **19**, 332001.
27 G. Korotcenkov and B. K. Cho, *Prog. Cryst. Growth Charact. Mater.*, 2012, **58**, 167–208.
28 A. Kolmakov and M. Moskovits, *Annu. Rev. Mater. Res.*, 2004, **34**, 151–180.
29 M. Tonezzer and N. V. Hieu, *Sens. Actuators, B*, 2012, **163**, 146–152.
30 Z. Xiong, H. Wang, N. Xu, H. Li, B. Fang, Y. Zhao, J. Zhang and C. Zheng, *Int. J. Hydrogen Energy*, 2015, **40**, 10049–10062.

31 A. Tricoli, M. Graf and S. E. Pratsinis, *Adv. Funct. Mater.*, 2008, **18**, 1969–1976.
32 S. Kumar, S. D. Lawaniya, S. Agarwal, Y.-T. Yu, S. R. Nelamarri, M. Kumar, Y. K. Mishra and K. Awasthi, *Sens. Actuators, B*, 2023, **375**, 132943.
33 J. Guo, J. Gan, H. Ruan, X. Yuan, C. Kong, Y. Liu, M. Su, Y. Liu, W. Liu, B. Zhang, Y. Zhang, G. Cheng and Z. Du, *Exploration*, 2022, **2**, 20220065.
34 D.-J. Yang, I. Kamienchick, D. Y. Youn, A. Rothschild and I.-D. Kim, *Adv. Funct. Mater.*, 2010, **20**, 4258–4264.
35 T. Chen, G. Z. Xing, Z. Zhang, H. Y. Chen and T. Wu, *Nanotechnology*, 2008, **19**, 435711.
36 R. C. Deus, J. A. Cortés, M. A. Ramirez, M. A. Ponce, J. Andres, L. S. R. Rocha, E. Longo and A. Z. Simões, *Mater. Res. Bull.*, 2015, **70**, 416–423.
37 Y. Xing, L.-X. Zhang, C.-T. Li, Y.-Y. Yin and L.-J. Bie, *Sens. Actuators, B*, 2022, **354**, 131220.
38 Y. Lin, P. Deng, Y. Nie, Y. Hu, L. Xing, Y. Zhang and X. Xue, *Nanoscale*, 2014, **6**, 4604–4610.
39 A. Sreedhar, I. Neelakanta Reddy, Q. T. H. Ta, G. Namgung and J.-S. Noh, *J. Electroanal. Chem.*, 2019, **832**, 426–435.
40 J. Liu, L. Zhang, J. Fan, B. Zhu and J. Yu, *Sens. Actuators, B*, 2021, **331**, 129425.
41 H. Liu, K. Tian, J. Ning, Y. Zhong, Z. Zhang and Y. Hu, *ACS Catal.*, 2019, **9**, 1211–1219.
42 K. D. Schierbaum, *Surf. Sci.*, 1998, **399**, 29–38.
43 L. Lv, P. Cheng, Y. Zhang, Y. Zhang, Z. Lei, Y. Wang, L. Xu, Z. Weng and C. Li, *Sens. Actuators, B*, 2022, **358**, 131490.
44 Y. Wang, X.-n. Meng and J.-l. Cao, *J. Hazard. Mater.*, 2020, **381**, 120944.
45 P. Jaroenapibal, P. Boonma, N. Saksilaporn, M. Horprathum, V. Amornkitbamrung and N. Triroj, *Sens. Actuators, B*, 2018, **255**, 1831–1840.
46 J.-B. Sun, W.-X. Liu, Y.-N. Li, B.-Y. Song, D.-R. Kong, J.-X. Ye, X.-F. Zhang, Z.-P. Deng, Y.-M. Xu, L.-H. Huo and S. Gao, *Sens. Actuators, B*, 2023, **375**, 132891.
47 E. Wongrat, N. Hongsith, D. Wongratanaphisan, A. Gardchareon and S. Choopun, *Sens. Actuators, B*, 2012, **171–172**, 230–237.
48 C. Xu, J. Tamaki, N. Miura and N. Yamazoe, *Sens. Actuators, B*, 1991, **3**, 147–155.
49 X. Wang, T. Wang, G. Si, Y. Li, S. Zhang, X. Deng and X. Xu, *Sens. Actuators, B*, 2020, **302**, 127165.
50 Y.-J. Li, K.-M. Li, C.-Y. Wang, C.-I. Kuo and L.-J. Chen, *Sens. Actuators, B*, 2012, **161**, 734–739.
51 P. Jaroenapibal, P. Boonma, N. Saksilaporn, M. Horprathum, V. Amornkitbamrung and N. Triroj, *Sens. Actuators, B*, 2018, **255**, 1831–1840.
52 C. W. Na, H.-S. Woo, I.-D. Kim and J.-H. Lee, *Chem. Commun.*, 2011, **47**, 5148–5150.
53 J. Zhang, X. Jia, T. Liu, J. Yang, S. Wang, Y. Li, D. Shao, L. Feng and H. Song, *Sens. Actuators, B*, 2022, **359**, 131601.
54 L. Yueyue, S. Siqi, W. Yilin, L. Fengmin, W. Hongtao, B. Jihao, L. Min and L. Geyu, *Sens. Actuators, B*, 2022, **368**, 132189.
55 Z. Yuan, Z. Feng, L. Kong, J. Zhan and X. Ma, *J. Alloys Compd.*, 2021, **865**, 158890.
56 J. Cao, S. Wang, H. Zhang and T. Zhang, *J. Alloys Compd.*, 2019, **799**, 513–520.
57 C. Gu, H. Huang, J. Huang, Z. Jin, H. Zheng, N. Liu, M. Li, J. Liu and F. Meng, *Sens. Actuators, A*, 2016, **252**, 96–103.
58 R. Moos, K. Sahner, M. Fleischer, U. Guth, N. Barsan and U. Weimar, *Sensors*, 2009, **9**, 4323–4365.
59 A. Tricoli, M. Righettoni and A. Teleki, *Angew. Chem., Int. Ed.*, 2010, **49**, 7632–7659.
60 A. Katoch, S.-W. Choi, H. W. Kim and S. S. Kim, *J. Hazard. Mater.*, 2015, **286**, 229–235.
61 N. Barsan and U. Weimar, *J. Electroceram.*, 2001, **7**, 143–167.
62 Z. U. Abideen, A. Katoch, J.-H. Kim, Y. J. Kwon, H. W. Kim and S. S. Kim, *Sens. Actuators, B*, 2015, **221**, 1499–1507.
63 O. Lupan, V. Postica, F. Labat, I. Ciofini, T. Pauporté and R. Adelung, *Sens. Actuators, B*, 2018, **254**, 1259–1270.
64 S. Agarwal, P. Rai, E. N. Gatell, E. Llobet, F. Güell, M. Kumar and K. Awasthi, *Sens. Actuators, B*, 2019, **292**, 24–31.
65 J. Zhang, H. Lu, C. Yan, Z. Yang, G. Zhu, J. Gao, F. Yin and C. Wang, *Sens. Actuators, B*, 2018, **264**, 128–138.
66 C. Wang, L. Yin, L. Zhang, D. Xiang and R. Gao, *Sensors*, 2010, **10**, 2088–2106.
67 S. Y. Sawant, J. Y. Kim, T. H. Han, S. A. Ansari and M. H. Cho, *New J. Chem.*, 2018, **42**, 1995–2005.